Giant Second-Harmonic Generation in Ferroelectric $NbOI_2$

Ibrahim Abdelwahab[1,2], Benjamin Tilmann[2], Yaze Wu[3,4], David Giovanni[5], Ivan Verzhbitskiy[3,4], Menglong Zhu[1], Rodrigo Berté[2,6], Fengyuan Xuan[4], Leonardo de S. Menezes[2,7], Goki Eda[3,4], Tze Chien Sum[5], Su Ying Quek[3,4,8,9], Stefan A. Maier[10,11,2*], Kian Ping Loh[1,4*]

[1] Department of Chemistry, National University of Singapore, Singapore, Singapore

[2] Chair in Hybrid Nanosystems, Nanoinstitute Munich, Faculty of Physics, Ludwig-Maxilimians-Universität München, Munich, Germany

[3] Department of Physics, National University of Singapore, Singapore, Singapore

[4] Centre for Advanced 2D Materials and Graphene Research Centre, National University of Singapore, Singapore, Singapore

[5] School of Physical and Mathematical Sciences, Nanyang Technological University, Singapore, Singapore

[6] Instituto de Física, Universidade Federal de Goiás, 74001-970 Goiânia-GO, Brazil

[7] Departamento de Física, Universidade Federal de Pernambuco, 50670-901 Recife-PE, Brazil

[8] NUS Graduate School, Integrative Sciences and Engineering Programme, National University of Singapore, Singapore 117456

[9] Department of Materials Science and Engineering, National University of Singapore, 9 Engineering Drive 1, Singapore 117575

[10] School of Physics and Astronomy, Monash University, Clayton Victoria 3800, Australia

[11] Department of Physics, Imperial College London, London SW7 2AZ, UK

*Corresponding authors. Email: Stefan.Maier@monash.edu (S. A. M.); chmlohkp@nus.edu.sg (K. P. L.)

Abstract

Implementing nonlinear optical components in nanoscale photonic devices is challenged by phase matching conditions requiring thickness in the order of hundreds of wavelengths and disadvantaged by the short optical interaction depth of nanometer-scale materials and weak photon-photon interactions. Here we report that ferroelectric $NbOI_2$ nanosheets exhibit giant SHG with conversion efficiencies that are orders of magnitude higher than commonly reported nonlinear crystals. The nonlinear response scales with layer thickness and is strain- and electrical-tunable; a record >0.2 % absolute SHG conversion efficiency and an effective NL susceptibility $\chi_{eff}^{(2)}$ in the order of 10^{-9} m V^{-1} are demonstrated at average pump intensity of 8 kW/cm^2. Due to the interplay between anisotropic polarization and excitonic resonance in $NbOI_2$, the spatial profile of the polarized SHG response can be tuned by the excitation wavelength. Our results represent a new paradigm for ultrathin, efficient NL optical components.

Materials lacking inversion symmetry have a non-vanishing second-order nonlinear (NL) optical susceptibility. When this is combined with a permanent polarization, they can exhibit strong second-harmonic generation (SHG)[1]. SHG refers to the frequency doubling of a light wave, and it is of paramount importance for applications, such as coherent light generation, NL auto- and cross-correlations, optical signal processing, and imaging[2-7]. Besides, SHG is an optimal tool to probe material properties, such as crystal symmetry, relative orientation, polar domains, magnetic ordering, surfaces, and quantum interference, to name a few[8-13]. However, the inherently weak photon-photon interactions in classical inversion-asymmetric materials demand high-intensity pumping, bulky interaction volumes, and complex phase-matching techniques to achieve appreciable SHG responses. This prevents the realization of miniature NL optical devices that can function at moderate input powers.

Two-dimensional (2D) ferroelectric (FE) materials (i.e., materials possessing a spontaneous electric polarization P_S) are a relatively new class of ultrathin materials with potential applications in memory devices[14]. Ferroelectricity breaks the material's inversion symmetry, thus 2D ferroelectrics are excellent candidates for realizing strong NL responses over nanometer-scale interaction lengths. Layered niobium oxide dihalides $NbOX_2$ (X = Cl, Br, I)[15-18] have a Peierls-distorted polar structure, due to their anisotropic bonding along the in-plane b and c directions: only the b direction is polar, giving rise to strongly anisotropic ferroelectricity. Our density functional perturbation theory (DFPT) calculations predicted very large in-plane FE and piezoelectric responses for the $NbOX_2$ family (P_S = 1.43 × 10^{-10} C m^{-1} and piezoelectric stress tensor element e_{22} = 31.6 × 10^{-10} C m^{-1} for $NbOI_2$ monolayer)[19]. Given that the SHG intensity is proportional to spontaneous polarization[20], $NbOX_2$ are therefore highly promising for exploring large second-order optical nonlinearities.

Here, we report that 20 nm thick $NbOI_2$ flakes exhibit ultra-strong, electrically tunable SHG with an absolute conversion efficiency of 0.006 %, which is orders of magnitude larger than values reported for other 2D materials[21-26], Weyl semimetals[27] and conventional NL materials[28-31]. Straining (~ 3 %) the crystal along the polar direction leads to a 35 times enhancement of the SHG efficiency, achieving effective SHG susceptibility $\chi_{eff}^{(2)}$ of 113 × 10^{-11} m V^{-1} and absolute conversion efficiency of > 0.2 %. The SHG response can be switched from highly anisotropic to isotropic by tuning the wavelength around the exciton resonance.

Results

Structure characterization

Centimeter-sized $NbOI_2$ single crystals were grown by chemical vapor transport (CVT) (refer to the Methods section for more details). The crystal structure of $NbOI_2$ was resolved using single-crystal X-ray diffraction (SC-XRD) measurements. Bulk $NbOI_2$ crystallizes in a monoclinic crystal structure with space group *C2* (Table S1 and Supplementary Crystallographic Information Files (CIFs) contain the crystallographic data). Each $NbOI_2$ layer is composed of NbO_2I_4 octahedra which link together by sharing the opposite I corners along the crystallographic *c* axis and by sharing the opposite O corners along the *b* axis, as shown in Figure 1a. A first order Peierls distortion occurs along the *c* axis[32], which leads to the dimerization of Nb atoms. Consequently, an alternation of short and long Nb–Nb bond distances occurs along the NbI_4 chain direction (Fig. 1b). Furthermore, there occurs a second order Peierls distortion along the *b* axis, through which the Nb ions displace off the center positions of the octahedra towards one of the bridging O atoms. As a result, an alternation of two unequal Nb–O bond lengths takes place (Fig. 1c), giving rise to spontaneous polarization. The Peierls distortions are energetically favorable as they lower the total electronic energy of

the $NbOI_2$ system (Supplementary Note S1). The Nb–Nb···Nb alternation is measured to be 3.17 and 4.35 Å while the Nb–O···Nb alternation is 1.82 and 2.10 Å along the *c* and *b* axes, respectively. The large Nb off-center polar displacement (~ 0.14 Å) along the *b* axis drives a robust in-plane FE polarization, which is among the highest P_s values in the 2D ferroelectrics family[19, 33].

Anisotropic band structure

The anisotropic band structure of $NbOI_2$ is responsible for its large anisotropic optical properties. Figure 2a displays the density functional theory (DFT)-calculated energy band structure of $NbOI_2$ monolayer with projection on atomic orbitals. The polar (Nb–O···Nb) and nonpolar (Nb–Nb···Nb) directions correspond to the Γ → Y and Γ → X directions in the reciprocal space (*k*-space), respectively. The bottom four conduction bands are denoted as c_1, c_2, c_3, and c_4 and arise primarily from Nb *d* orbitals. The top four valence bands are denoted as v_1, v_2, v_3, and v_4. While most of the valence bands are attributed to I *p* orbitals, the highest energy valence band v_1 arises from Nb $d_{x^2-y^2}$ and Nb d_{z^2} orbitals, as a result of the splitting of the Nb $d_{x^2-y^2}/d_{z^2}$ bands due to Peierls distortion (Supplementary Note S1). Strikingly, there is strong mixing between the $d_{x^2-y^2}$ and d_{z^2} orbitals in v_1 and c_3 throughout the entire Brillouin zone. The material has fully occupied valence bands and the nearly flat v_1 band implies that the v_1 electrons are highly localized. The GW[34, 35]-calculated band structure of $NbOI_2$ (Supplementary Fig. S1) indicates that the valence band maximum occurs at *Y*, while the conduction band minimum occurs at *X* (within the c_2 band), giving an indirect bandgap (E_g = 2.24 eV).

The band structure is more dispersive along the polar direction than the nonpolar direction. As *k* varies from Γ to Y, the magnitude of the π-bond overlap between the Nb d_{yz} (d_{xy}) and O p_z

(p_x) orbitals increases quite substantially, bringing about highly dispersive c_1 and c_2 bands. The c_1 and c_2 bands are nevertheless weakly dispersive on going from Γ to X. This is due to the opposing effects of the metal–metal (Nb d_{yz}–Nb d_{yz}) and metal-ligand (Nb d_{yz}–I p_y) π-bond interactions at X as well as the weak Nb d_{xy}–Nb d_{xy} δ-bond interaction[36]. Similarly, the v_2 band varies rapidly in energy from Γ to Y and smoothly from Γ to X. We have carried out angle-resolved photoemission spectroscopy (ARPES) measurements to confirm the band structure of $NbOI_2$. The valence-band ARPES spectra of $NbOI_2$ clearly show the dispersive feature of the v_2 band along Γ-Y and the dispersionless feature of the bands along Γ-X (Fig. 2b); in good agreement with the band-structure calculations. A comparison of the ARPES results with the GW band structure shows good quantitative agreement; the similar valence band structure between monolayer (theory) and bulk (experiment) $NbOI_2$ indicates that the band dispersion does not vary with thickness, which is different from transition metal dichalcogenides (TMDs) and graphene. Interlayer interactions in bulk $NbOI_2$ induce band splitting for the bands that arise from out-of-plane orbitals (Supplementary Fig. S2). This can explain the broadening observed for some bands in the ARPES band structure.

Linear optical response

In line with its anisotropic band structure, the linear optical properties of $NbOI_2$ along the polar and non-polar directions are markedly different, which are confirmed by performing Mueller matrix ellipsometry measurements over a wide spectral range (6.2-0.65 eV, 200–1900 nm). The extracted imaginary part of the dielectric function (ε_2) is shown in Fig. 2c. We observe two predominant peaks confined along the nonpolar direction in the visible range (at P_1 = 2.34 eV/530 nm and P_2 = 2.64 eV/470 nm) and one broad peak confined along the polar direction in the near ultraviolet range (at P_4 = 3.54 eV/350 nm). According to our GW-BSE calculations, peaks P_1 to P_4 are excitonic in nature. The presence of strong optical anisotropy is also reflected from polarization-dependent absorption and transmission measurements (Supplementary Fig.

S3, Fig. S4, and Movie S1). In line with the ellipsometry data, two absorption peaks at ~ 530 nm and 470 nm are detected when light is linearly polarized along the nonpolar direction of $NbOI_2$ (Supplementary Fig. S3). In contrast, a much weaker absorption in the visible range is collected when light is polarized along the polar direction. Moreover, no circular dichroism signal was observed under circular optical excitation (Supplementary Fig. S5), excluding any optical activity (chirality) in $NbOI_2$.

Nonlinear optical response

We isolate $NbOI_2$ flakes of sub-100 nm thicknesses from a single crystal for NL optical study. The $NbOI_2$ nanosheets were encapsulated with a thin layer of transparent hexagonal boron nitride (h-BN) to avoid any photo-oxidation effects. For space group C2, there are eight non-vanishing SHG tensor elements: d_{14}, d_{16}, d_{21}, d_{22}, d_{23}, d_{25}, d_{34}, and d_{36} (Supplementary Note S2), where the SHG susceptibility $\chi_{ijk}^{(2)}$ can be calculated by $\chi_{ijk}^{(2)} = 2d_{ij}$. Considering the Kleinman symmetry, $d_{16} = d_{21}$; $d_{14} = d_{25} = d_{36}$; and $d_{23} = d_{34}$, the spontaneous polarization in $NbOI_2$ induces an extremely large d_{22} coefficient (i.e., the SHG tensor element along the polar axis). To selectively probe the d_{22} coefficient, we pumped $NbOI_2$ nanosheets supported on a quartz substrate (Figure 3a) with normally incident (along the a axis) femtosecond laser pulses whose linear polarization is parallel to the polar direction of $NbOI_2$. Figure 3b shows resultant SHG intensity maps of the sample at two representative SHG wavelengths (λ_{SHG} = 450 and 500 nm). Notably, a highly efficient SHG signal covering the region of λ_{SHG} = 425–525 nm is detected for the $NbOI_2$ flakes (Fig. 3b and Supplementary Fig. S6), with negligible background contribution from the quartz substrate. The strong broadband d_{22}-SHG emission attained at low optical pumping losses (refer to the red curve in Fig. 2c) is a direct consequence of the large ferroelectricity of $NbOI_2$. When the excitation wavelength is detuned below λ_{pump} = 800 nm, we find that the SHG emission intensity is reduced significantly, and the two-photon

absorption (2PA) process emerges (Supplementary Fig. S7). This is anticipated, as the excitation photon energy is high enough ($\hbar\omega > \frac{1}{2}E_g$) to allow 2PA to populate the conduction band of $NbOI_2$ and, as a result, the slow band-to-band 2PA nonlinearity greatly outweighs the instantaneous SHG nonlinearity[1].

In accordance with the second-order nature of the process, the generated SHG power in $NbOI_2$ maintains a quadratic dependence on the average input laser power up to ~ 80 μW (2.2 kW peak power, λ_{pump} = 1050 nm), as shown in Fig. 3c for 20 nm-thick $NbOI_2$. Neither saturation nor hysteresis behavior in the SHG profile was observed up to the maximum input power used, ruling out any laser-induced material damage. In addition to their thermal stability under laser illumination, the optical properties of $NbOI_2$ flakes show remarkable air stability over several months (Supplementary Fig. S8). Remarkably, an absolute SHG conversion efficiency (η_{SHG}), calculated as the ratio between SHG and excitation powers ($\eta_{SHG} = P_{SHG}/P_{Pump}$), of ~ 0.006 % is attained for the $NbOI_2$ nanoflakes at λ_{pump} = 1050 nm (η_{SHG} is on the order of 0.0001% for $NbOI_2$ monolayer), which is orders of magnitude higher than the values previously reported for other NL 2D materials (Supplementary Table 2). The measured SHG efficiency (0.006 %) at 1000-1050 nm excitation is also orders of magnitude higher than that reported for $NbOI_2$ flake of similar thickness excited by 1200 nm pump in Ref. [37] ($191\times\eta_{MoS2} \approx 10^{-6}$ %). As shown in Supplementary Fig. 6, The SHG response significantly drops for input wavelengths above 1050 nm.

The effective bulk-like SHG susceptibility $\chi^{(2)}_{eff}$ of $NbOI_2$ can be obtained by dividing the SHG sheet susceptibility $\chi^{(2)}_{s}$ (as calculated in Ref. [26]) by the $NbOI_2$ flake thickness. We estimate an $\chi^{(2)}_{eff}$ of ~ 19 $\times 10^{-11}$ m V^{-1}, which is larger than those of commonly used nonlinear crystals (e.g.,

$LiNbO_3$ with 5.2×10^{-11} m V^{-1}). This is corroborated by the large d_{22}-SHG coefficients that we have calculated within the independent particle approximation using DFT (Supplementary Note S3 and Supplementary Fig. S9). The calculations predict large d_{22}-SHG coefficients corresponding to outgoing photon energies in the range ~ 2.0-2.6 eV (peaks B-C), as well as ~ 1.3-1.5 eV (peak A). The interband transitions giving rise to these peaks are shown in Supplementary Table S3. We expect that electron self-energy effects will blue shift these peaks, while excitonic effects may increase the maximum SHG amplitudes.

The AB Bernal stacking of many 2D materials (e.g., the 2H phases of group VI TMDs) results in ultrathin flakes with thickness corresponding to even-layer number unit cells to be inversion symmetric and SHG-inactive, and only ultrathin flakes with thickness corresponding to odd-layer number unit cells can be SHG-active. This effectively constrains the NL response to atomically thin interaction lengths for many TMD materials that possess bulk inversion symmetry. In contrast, $NbOI_2$ has a broken inversion symmetry regardless of thickness and its SHG response scales with thickness. Taking into consideration the coherence length of the generated SHG radiation and interference effects[38, 39], the $\chi_s^{(2)}$ of AA-stacked $NbOI_2$ scales with thickness (Supplementary Fig. S10), rendering $NbOI_2$ practically useful for highly efficient parametric conversion processes. Moreover, SHG can be used for the non-invasive visualization of nanoscale $NbOI_2$ FE domains that are otherwise challenging to probe (Supplementary Note S4). The white arrows in Supplementary Fig. S11 point out 180° domain walls separating oppositely polarized FE domains.

To probe the spatial dependence of the NL response, the total SHG intensity (i.e., without an analyzing polarizer in the detection channel) is measured as a function of the input laser polarization. Figure 3d shows the SHG intensity maps of the $NbOI_2$ sample with excitation laser polarized along the nonpolar direction. The results reveal that, outside the nonpolar P_1–

P_2 excitonic bands (consider the examples of λ_{SHG} = 450 nm in Figs. 3b and 3d and λ_{SHG} = 750 nm in Supplementary Fig. S12), d_{22} is the dominant coefficient of $\chi^{(2)}$ which leads to a dominant SHG signal for input light polarized in the polar direction as manifested in the anisotropic two-lobed SHG intensity pattern (Fig. 3e). The ratio of SHG intensities along the two in-plane axes exceeds 7 for λ_{SHG} = 450 nm. However, when the generated SHG signal is resonant with the energy of the P_1 and P_2 excitons (e.g., λ_{SHG} = 525 nm), the strong resonance and localization effects greatly magnify the d_{16} coefficient, enhancing the SHG signal for input light polarized in the nonpolar direction to be comparable with the polar signal and resulting in an isotropic, near-circular SHG intensity pattern. The SHG polar plots in Fig. 3e and the polar and nonpolar SHG signals in Fig. 3f clearly display this wavelength-dependent SHG anisotropy-isotropy crossover. This contrasts with group VI TMDs (e.g., 2H-MoS_2) showing only isotropic SHG polar plots and group VII TMDs (e.g., ReS_2) showing only anisotropic SHG polar plots for the total SHG intensity[40, 41]. The polarization of the emitted SHG signal is also analyzed and found to be strongly polarized along the nonpolar direction, regardless of the excitation polarization (Supplementary Note S5 and Supplementary Fig. S13).

Manipulation of the nonlinear response

The structural polarity of $NbOI_2$ and, consequently, its NL response, can be strongly modulated using external stimuli such as mechanical strain, temperature, or external electric field. Theoretically, the Nb polar displacement can be increased twofold by applying 3 % tensile strain along the polar axis. The strong piezoelectric response predicted for $NbOI_2$[19] should lead to a strong built-in piezoelectric field and enhanced SHG signal in strained $NbOI_2$. To validate this, we introduced a localized uniaxial strain along the polar direction *via* the buckling-induced delamination process[42]. Figure 4a and Supplementary Fig. S14 depict buckling-induced $NbOI_2$ wrinkles separated by flat unstrained regions. The maximum tensile strain at the crest of the

wrinkles is quantified by means of linear buckling theory and atomic force microscopy (AFM) characterization (Supplementary Note S6 and Supplementary Fig. S15). The presence of both curved and flat areas in the same $NbOI_2$ flake allows their NL optical properties to be compared. We mapped the SHG intensity as a function of the spatial position of the sample with the pump polarized along the polar axis. As illustrated in Fig. 4a, in comparison to the flat areas, the $NbOI_2$ wrinkled regions (3.1 % strain) show up to a 35-fold increase in the SHG intensity, reaching a record efficiency η_{SHG} of > 0.2 % ($\chi_{eff}^{(2)}$ ~ 113×10^{-11} m V^{-1}). In addition, the SHG polar plot of the strained area reveals that the isotropic SHG response (within the nonpolar exciton band) vanishes due to the lengthening of the d_{22} coefficient (Fig. 4b). The high NL conversion efficiency of $NbOI_2$ motivates multiple applications in classical and quantum photonics. For example, it can be utilized as an ultrathin pump for parametric down-converters to produce high-flux squeezed and entangled quantum states of light, with applications in quantum computation and quantum cryptography[43-45]. Besides the strain engineering of the NL response, the SHG intensity increases 5 times (Fig. 4c) by reducing the temperature to 78 K, implying an enhanced FE polarization. This is further confirmed by low temperature SC-XRD measurements (Supplementary CIFs), showing that the Nb polar displacement extends from 0.14 Å at 298 K to 0.17 Å at 100 K.

The spontaneous polarization of a FE material, by definition, can be switched by an external electric field. The ferroelectric property of $NbOI_2$ is verified from its polarization *versus* electric field ($P-E$) characteristics (Fig. 4d) measured when an external electric field is applied along the polar direction. The curve exhibits a clear ferroelectric hysteresis loop (Supplementary Note S7). The coercive field E_c and saturation field E_{sat} are determined to be ~ ± 8.5 kV/cm and ± 17.5 kV/cm, respectively. In order to study the dynamic properties of d_{22}-SHG, we monitor the SHG intensity as a function of the applied in-plane electric field, as shown

in Fig. 4e for the positive electric field part. The SHG intensity increases rapidly once the coercive field threshold is overcome and eventually saturates, following the same trend as the polarization. The large modulation contrast (≥ 80 %) of the SHG signal between two states (paraelectric at E_c and monodomain ferroelectric at E_{sat}) by electric field can potentially enable electrically tunable integrated light sources (e.g., frequency combs) for sensing and on-chip communication[46, 47]. Similar dynamic control over the SHG signal is registered in the negative applied field region (Supplementary Fig. S16), affirming the polar switchability in $NbOI_2$ at room temperature. The polarization reversal (domain switching) in $NbOI_2$ implies that the sign of the NL coefficient can be periodically reversed along the interaction length. This deterministic control of the sign and magnitude of the NL coefficient at the nanoscale opens up a promising area for designing optical modulators and transistor devices with high SHG efficiencies for optical signal processing[48-50].

Conclusion and outlook

We demonstrate that polar 2D $NbOI_2$ shows a very strong second order parametric response. The strongly piezoelectric nature of $NbOI_2$ allows strain-tunable NL response with a record SHG absolute conversion efficiency of >0.2% without purposefully considering phase matching conditions. The spatial profile of the polarized SHG response can be modulated by resonance or off-resonance excitations, as well as strain. Taking advantage of the switchable ferroelectric polarization of $NbOI_2$, the SHG signal can be electrically modulated with modulation contrast exceeding 80 %. Our work suggests that polar layered transition metal oxidehalides that combine strong piezoelectric and FE properties allow strain and polar order to be coupled with NL responses, enabling a new generation of strain-tunable and electrical-tunable NL optical devices.

Acknowledgments
I.A. acknowledges funding support through a Humboldt Research Fellowship from the Alexander von Humboldt Foundation. K.P.L. acknowledges support from the Singapore National Research Foundation (NRF), Competitive Research Program NRF-CRP22-2019-0006, Prime Minister's Office, Singapore. T.C.S. acknowledges support from the Ministry of Education (MOE), Singapore, under AcRF Tier 2 grant (MOE2019-T2-1-006). G.E. acknowledges support from MOE, Singapore, under AcRF Tier 3 grant (MOE2018-T3-1-005) and the Singapore NRF for funding the research under medium-sized centre programme. The authors would like to acknowledge the Singapore Synchrotron Light Source (SSLS) for providing the facility necessary for conducting the Mueller matrix ellipsometry measurements. S.A.M. acknowledges LMUexcellent, the Deutsche Forschungsgemeinschaft (DFG, German Research Foundation) under Germany's Excellence Strategy – EXC 2089/1 – 390776260, the EPSRC Reactive Plasmonics Programme EP/M013812/1, and the Lee Lucas Chair in Physics.

Author contributions
I.A., S.A.M. and K.P.L. conceived the project and designed the experiments. I.A. performed micromechanical cleavage, 2D dry transfer, device fabrication and material characterization under the supervision of S.A.M. and K.P.L.. I.A., B.T., D.G. and R.B. performed all the optical characterizations under the guidance of L.d.S.M., T.C.S., S.A.M. and K.P.L.. Y.W. and F.X. performed the calculations and theoretical analysis under supervision of S.Y.Q.. I.V. synthesized the $NbOI_2$ bulk crystals under the supervision of G.E.. M.Z. performed the ARPES measurement. I.A. wrote the manuscript with input from all authors.

Competing interests
The authors declare no competing interests.

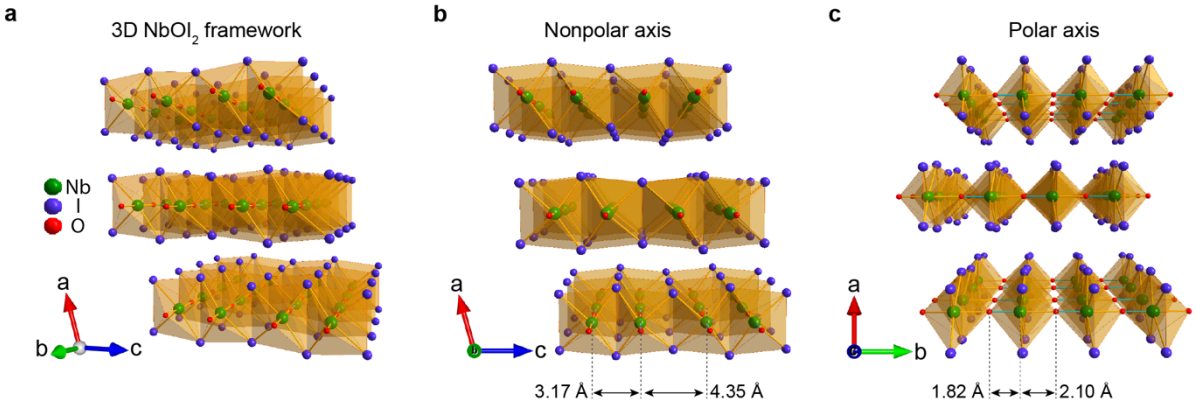

Fig. 1 | Atomic structure of ferroelectric layered $NbOI_2$. a, Three-dimensional schematic diagram of trilayer $NbOI_2$ monoclinic crystal structure (space group *C2*). Each $NbOI_2$ layer is composed of NbO_2I_4 octahedra linked together by sharing the opposite I corners along the crystallographic *c* axis and by sharing the opposite O corners along the *b* axis. **b**, A side view of trilayer $NbOI_2$ along the nonpolar *c* axis showing an alternation of short and long Nb–Nb distances. **c**, A side view of trilayer $NbOI_2$ along the polar *b* axis showing an alternation of two unequal Nb–O bond lengths. The Nb–Nb···Nb alternation is 3.17 and 4.35 Å while the Nb–O···Nb alternation is 1.82 and 2.10 Å along the *c* and *b* axes, respectively. The thickness of $NbOI_2$ monolayer is 0.73 nm

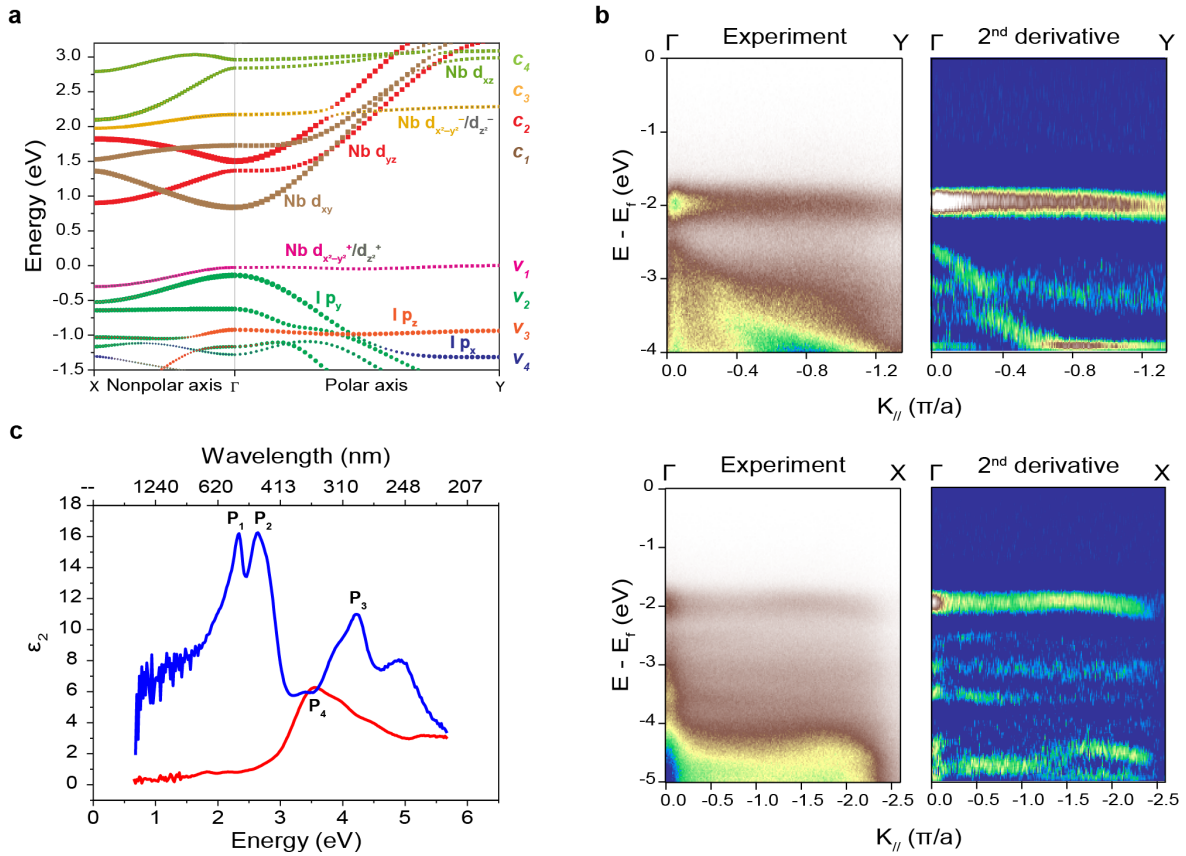

Fig. 2 | Anisotropic band structure and linear optical response of $NbOI_2$. a, DFT calculated band structure of $NbOI_2$ monolayer. The Γ → Y and Γ → X high-symmetry directions in the reciprocal space (k-space) correspond respectively to the polar (Nb–O···Nb) and nonpolar (Nb–Nb···Nb) directions of $NbOI_2$ in real space. The valence band maximum is set to zero energy. Orbital component analysis is elucidated by different colors: v_1 (magenta/gray, Nb orbital $d_{x^2-y^{2+}}/d_{z^{2+}}$), v_2 (green, I orbital p_y), v_3 (orange, I orbital p_z), v_4 (blue, I orbital p_x); c_1 (brown, Nb orbital d_{xy}), c_2 (red, Nb orbital d_{yz}), c_3 (yellow/gray, Nb orbital $d_{x^2-y^{2-}}/d_{z^{2-}}$), c_4 (olive, Nb orbital d_{xz}). The + and – subscripts for the Nb $d_{x^2-y^2}$ and Nb d_{z^2} orbitals refer to the energy-split v_1 (+) and c_3 (–) Nb $d_{x^2-y^2}/d_{z^2}$ bands due to Peierls distortion. The x, y, z directions correspond, respectively, to the a, b, c crystal axes of the $NbOI_2$ unit cell. **b**, ARPES intensity plots and their corresponding second-derivative plots of $NbOI_2$ along the polar (top) and nonpolar (bottom) directions, where $k_{//}$ is the in-plane component of electron momentum. Fermi level is at zero energy. **c**, The imaginary dielectric function ε_2 of $NbOI_2$ along the polar (red) and nonpolar (blue) directions, obtained by Mueller matrix ellipsometry measurements. Our GW-BSE calculations reveal that the P_1 and P_2 excitons arise from transitions from v_1, v_2 and v_3 to c_1.

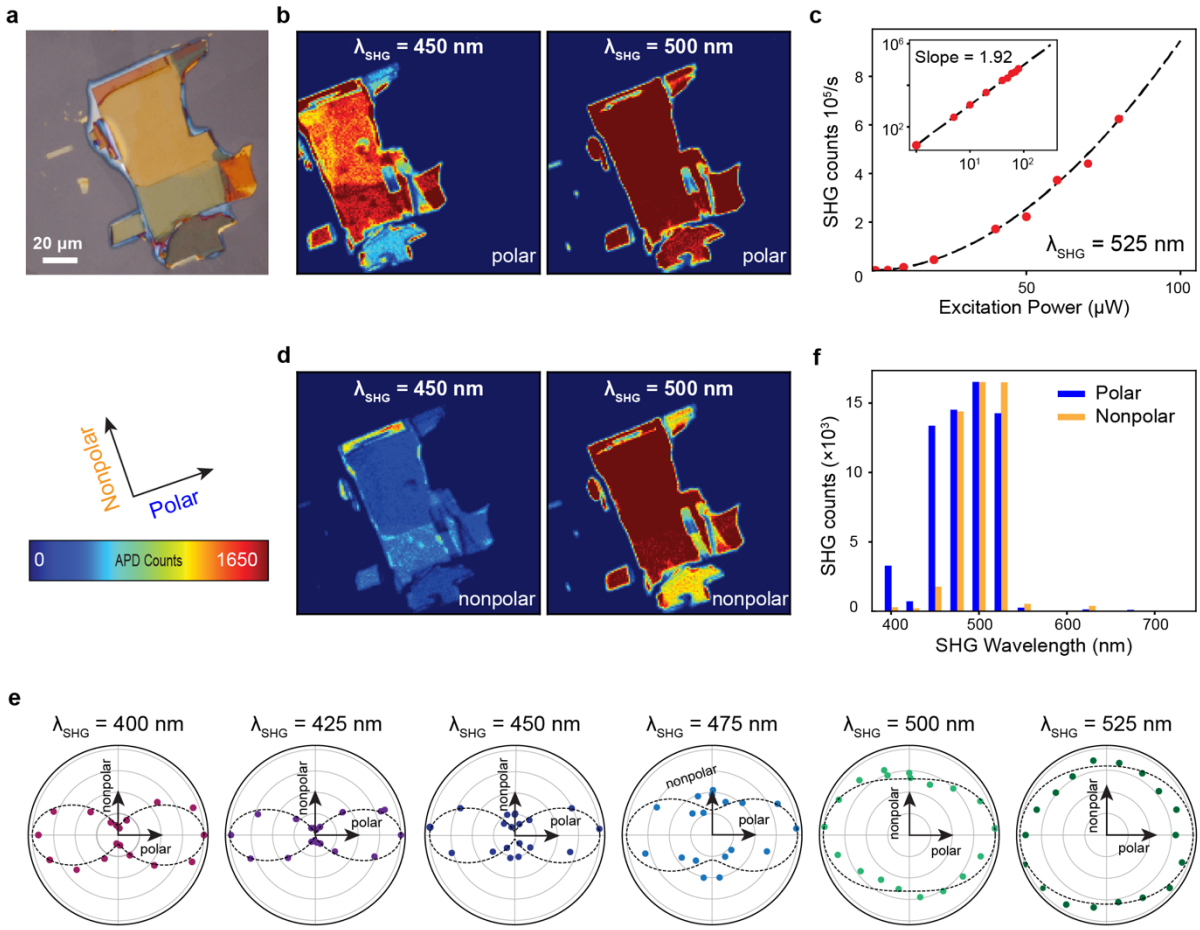

Fig. 3 | Characterization of second-harmonic generation (SHG) in $NbOI_2$. a, Optical image of $NbOI_2$ flake on quartz substrate after encapsulation with *h*-BN. **b**, SHG intensity maps recorded with an avalanche photodiode (APD) of the sample shown in **a** at λ_{SHG} = 450 nm and 500 nm obtained by setting the excitation polarization parallel to the polar direction of $NbOI_2$. **c**, Excitation power dependence of the SHG signal (red dots) with quadratic fit (dash curve) at λ_{SHG} = 525 nm for 20-nm-thick $NbOI_2$ flake. The inset shows the linear fit of the log-log plot with a slope equal to 1.92. **d**, SHG intensity maps of the sample in **a** at λ_{SHG} = 450 nm and 500 nm obtained by setting the excitation polarization parallel to the nonpolar direction of $NbOI_2$. All the maps in **b** and **d** are acquired using equally intense excitation pulses. **e**, Polar plots of the total SHG intensity as a function of the polarization angle of the excitation beam at λ_{SHG} = 400–525 nm. The colored dots represent the experimental data while the dash lobes represent the theoretical (considering the Kleinman symmetry) predictions of the SHG intensity as a function of the input polarization. **f**, Bar chart showing the polar and nonpolar SHG signals from $NbOI_2$ flake in the range of λ_{SHG} = 400–750 nm while maintaining constant excitation intensities. The polar SHG signal is 7.6 times the non-polar signal at 450 nm, but their signals reach similar intensities between 475 to 525 nm.

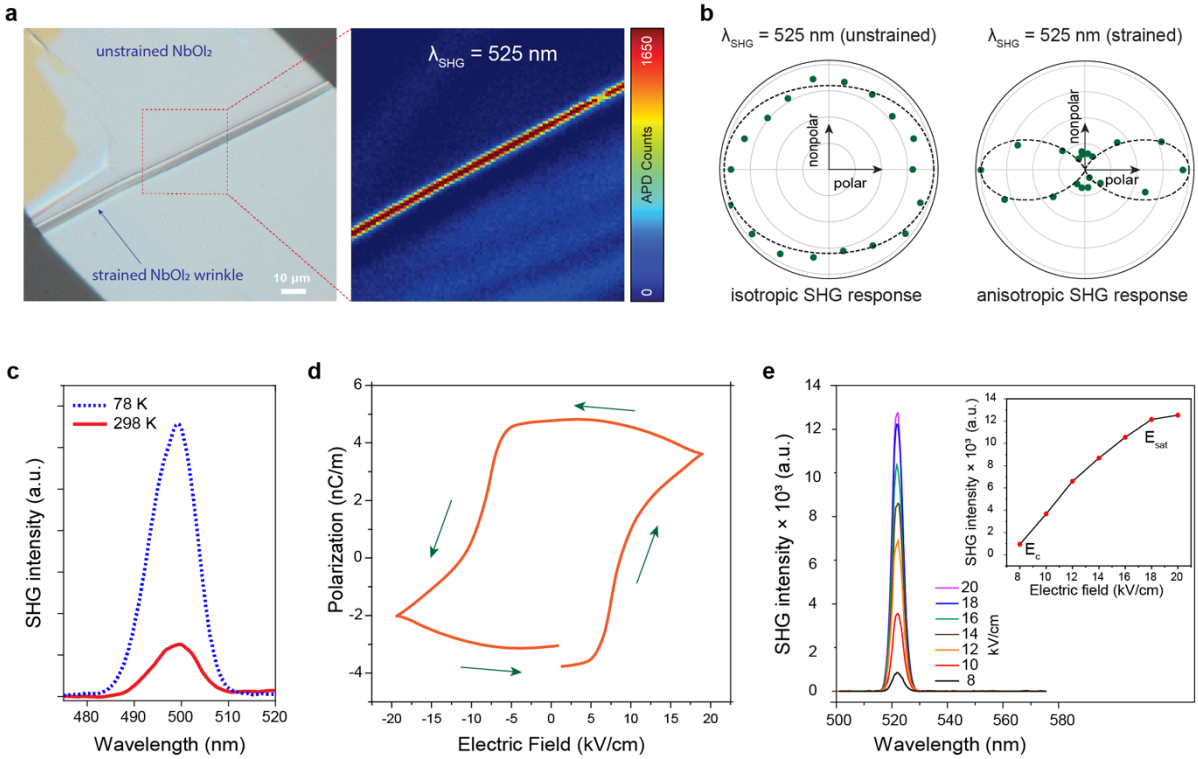

Fig. 4 | Effects of strain, temperature and electric fields on SHG in $NbOI_2$. a, Optical image of wrinkled $NbOI_2$ flake (left), and corresponding SHG map at λ_{SHG} = 525 nm (right). **b**, Polar plots of the total SHG intensity as a function of the polarization angle of the excitation beam at λ_{SHG} = 525 nm for the flat and strained $NbOI_2$ regions. **c**, Temperature-dependent SHG at 298 K (red solid line) and 78 K (blue dashed line). **d**, Polarization *versus* electric field ($P - E$) hysteresis loop of $NbOI_2$ nanosheet at room temperature. **e**, SHG spectra as a function of the external electric field strength. An in-plane electric field is applied along the polar direction of the $NbOI_2$ nanosheet. The fundamental wavelength is 1050 nm. The inset shows the peak SHG intensity as a function of external electric field strength.

References

1. Boyd RW. *Nonlinear optics*, 3rd edn. Academic Press: Burlington, MA, 2008.

2. Helk T, Berger E, Jamnuch S, Hoffmann L, Kabacinski A, Gautier J, *et al.* Table-top extreme ultraviolet second harmonic generation. *Science Advances* 2021, **7**(21)**:** eabe2265.

3. Shwartz S, Fuchs M, Hastings J, Inubushi Y, Ishikawa T, Katayama T, *et al.* X-ray second harmonic generation. *Phys Rev Lett* 2014, **112**(16)**:** 163901.

4. Trebino R, DeLong KW, Fittinghoff DN, Sweetser JN, Krumbügel MA, Richman BA, *et al.* Measuring ultrashort laser pulses in the time-frequency domain using frequency-resolved optical gating. *Review of Scientific Instruments* 1997, **68**(9)**:** 3277-3295.

5. Willner AE, Khaleghi S, Chitgarha MR, Yilmaz OF. All-Optical Signal Processing. *J Lightwave Technol* 2014, **32**(4)**:** 660-680.

6. Pantazis P, Maloney J, Wu D, Fraser SE. Second harmonic generating (SHG) nanoprobes for in vivo imaging. *Proceedings of the National Academy of Sciences* 2010, **107**(33)**:** 14535-14540.

7. Manaka T, Lim E, Tamura R, Iwamoto M. Direct imaging of carrier motion in organic transistors by optical second-harmonic generation. *Nat Photonics* 2007, **1**(10)**:** 581-584.

8. Yin X, Ye Z, Chenet DA, Ye Y, O'Brien K, Hone JC*, et al.* Edge Nonlinear Optics on a MoS_2 Atomic Monolayer. *Science* 2014, **344**(6183)**:** 488-490.

9. Shen Y. Surface properties probed by second-harmonic and sum-frequency generation. *Nature* 1989, **337**(6207)**:** 519-525.

10. Hsieh D, McIver J, Torchinsky DH, Gardner DR, Lee YS, Gedik N. Nonlinear optical probe of tunable surface electrons on a topological insulator. *Phys Rev Lett* 2011, **106**(5)**:** 057401.

11. Yakovlev DR, Pavlov VV, Rodina AV, Pisarev RV, Mund J, Warkentin W*, et al.* Exciton Spectroscopy of Semiconductors by the Method of Optical Harmonics Generation (Review). *Physics of the Solid State* 2018, **60**(8)**:** 1471-1486.

12. Chauleau J-Y, Haltz E, Carrétéro C, Fusil S, Viret M. Multi-stimuli manipulation of antiferromagnetic domains assessed by second-harmonic imaging. *Nature materials* 2017, **16**(8)**:** 803-807.

13. Lin K-Q, Bange S, Lupton JM. Quantum interference in second-harmonic generation from monolayer WSe_2. *Nature Physics* 2019, **15**(3)**:** 242-246.

14. Cui C, Xue F, Hu W-J, Li L-J. Two-dimensional materials with piezoelectric and ferroelectric functionalities. *npj 2D Materials and Applications* 2018, **2**(1)**:** 1-14.

15. Schäber H, Gerken R. Beiträge zur Chemie der Elemente Niob und Tantal. XXIX. $NbOJ_3$ und $NbOJ_2$. Darstellung, Eigenschaften und thermisches Verhalten. *Zeitschrift für anorganische und allgemeine Chemie* 1962, **317**(1-2)**:** 105-112.

16. Rijnsdorp J, Jellinek F. The crystal structure of niobium oxide diiodide $NbOI_2$. *Journal of the Less Common Metals* 1978, **61**(1)**:** 79-82.

17. Hillebrecht H, Schmidt P, Rotter H, Thiele G, Zönnchen P, Bengel H*, et al.* Structural and scanning microscopy studies of layered compounds MCl_3 (M= Mo, Ru, Cr) and $MOCl_2$ (M= V, Nb, Mo, Ru, Os). *Journal of alloys and compounds* 1997, **246**(1-2)**:** 70-79.

18. Beck J, Kusterer C. Crystal Structure of $NbOBr_2$. *Zeitschrift für anorganische und allgemeine Chemie* 2006, **632**(14)**:** 2193-2194.

19. Wu Y, Abdelwahab I, Kwon KC, Verzhbitskiy I, Wang L, Liew WH*, et al.* Data-driven discovery of high performance layered van der Waals piezoelectric $NbOI_2$. *Nat Commun* 2022, **13**(1)**:** 1884.

20. Pugachev A, Kovalevskii V, Surovtsev N, Kojima S, Prosandeev S, Raevski I*, et al.* Broken local symmetry in paraelectric $BaTiO_3$ proved by second harmonic generation. *Phys Rev Lett* 2012, **108**(24)**:** 247601.

21. Clark D, Le C, Senthilkumar V, Ullah F, Cho H-Y, Sim Y*, et al.* Near bandgap second-order nonlinear optical characteristics of MoS_2 monolayer transferred on transparent substrates. *Applied Physics Letters* 2015, **107**(13)**:** 131113.

22. Woodward R, Murray R, Phelan C, de Oliveira R, Runcorn T, Kelleher E*, et al.* Characterization of the second-and third-order nonlinear optical susceptibilities of monolayer MoS_2 using multiphoton microscopy. *2D Mater* 2016, **4**(1)**:** 011006.

23. Säynätjoki A, Karvonen L, Rostami H, Autere A, Mehravar S, Lombardo A*, et al.* Ultra-strong nonlinear optical processes and trigonal warping in MoS_2 layers. *Nat Commun* 2017, **8**(1)**:** 1-8.

24. Seyler KL, Schaibley JR, Gong P, Rivera P, Jones AM, Wu S*, et al.* Electrical control of second-harmonic generation in a WSe_2 monolayer transistor. *Nat Nanotechnol* 2015, **10**(5)**:** 407.

25. Karvonen L, Säynätjoki A, Mehravar S, Rodriguez RD, Hartmann S, Zahn DRT*, et al.* Investigation of second- and third-harmonic generation in few-layer gallium selenide by multiphoton microscopy. *Sci Rep* 2015, **5**(1)**:** 10334.

26. Malard LM, Alencar TV, Barboza APM, Mak KF, de Paula AM. Observation of intense second harmonic generation from MoS_2 atomic crystals. *Phys Rev B* 2013, **87**(20)**:** 201401.

27. Wu L, Patankar S, Morimoto T, Nair NL, Thewalt E, Little A*, et al.* Giant anisotropic nonlinear optical response in transition metal monopnictide Weyl semimetals. *Nature Physics* 2017, **13**(4)**:** 350-355.

28. Bergfeld S, Daum W. Second-Harmonic Generation in GaAs: Experiment versus Theoretical Predictions of $\chi^{(2)}_{xyz}$. *Phys Rev Lett* 2003, **90**(3)**:** 036801.

29. Shoji I, Kondo T, Kitamoto A, Shirane M, Ito R. Absolute scale of second-order nonlinear-optical coefficients. *JOSA B* 1997, **14**(9)**:** 2268-2294.

30. Yariv A, Yeh P. *Photonics: optical electronics in modern communications*. Oxford university press, 2007.

31. Shen Y-R. The principles of nonlinear optics. *New York* 1984.

32. Peierls RE. *Quantum theory of solids*. Clarendon Press, 1996.

33. Jia Y, Zhao M, Gou G, Zeng XC, Li J. Niobium oxide dihalides $NbOX_2$: a new family of two-dimensional van der Waals layered materials with intrinsic ferroelectricity and antiferroelectricity. *Nanoscale Horizons* 2019, **4**(5)**:** 1113-1123.

34. Hedin L. New Method for Calculating the One-Particle Green's Function with Application to the Electron-Gas Problem. *Physical Review* 1965, **139**(3A)**:** A796-A823.

35. Hybertsen MS, Louie SG. Electron correlation in semiconductors and insulators: Band gaps and quasiparticle energies. *Physical Review B* 1986, **34**(8)**:** 5390-5413.

36. Rouxel J. *Crystal Chemistry and Properties of Materials with Quasi-One-Dimensional Structures: A Chemical and Physical Synthetic Approach*. D. Reidel Publishing Company, 1986.

37. Fang Y, Wang F, Wang R, Zhai T, Huang F. 2D $NbOI_2$: A Chiral Semiconductor with Highly In-Plane Anisotropic Electrical and Optical Properties. *Adv Mater* 2021, **33**(29)**:** 2101505.

38. Bloembergen N, Pershan PS. Light Waves at the Boundary of Nonlinear Media. *Physical Review* 1962, **128**(2)**:** 606-622.

39. Hopfield JJ, Thomas DG. Theoretical and Experimental Effects of Spatial Dispersion on the Optical Properties of Crystals. *Physical Review* 1963, **132**(2)**:** 563-572.

40. Li Y, Rao Y, Mak KF, You Y, Wang S, Dean CR*, et al.* Probing symmetry properties of few-layer MoS_2 and h-BN by optical second-harmonic generation. *Nano letters* 2013, **13**(7)**:** 3329.

41. Song Y, Hu S, Lin M-L, Gan X, Tan P-H, Zhao J. Extraordinary Second Harmonic Generation in ReS_2 Atomic Crystals. *ACS Photonics* 2018, **5**(9)**:** 3485-3491.

42. Vella D, Bico J, Boudaoud A, Roman B, Reis PM. The macroscopic delamination of thin films from elastic substrates. *Proceedings of the National Academy of Sciences* 2009, **106**(27)**:** 10901-10906.

43. Fickler R, Lapkiewicz R, Plick WN, Krenn M, Schaeff C, Ramelow S*, et al.* Quantum Entanglement of High Angular Momenta. *Science* 2012, **338**(6107)**:** 640-643.

44. Fedrizzi A, Herbst T, Poppe A, Jennewein T, Zeilinger A. A wavelength-tunable fiber-coupled source of narrowband entangled photons. *Opt Express* 2007, **15**(23)**:** 15377-15386.

45. Zhang G, Haw JY, Cai H, Xu F, Assad SM, Fitzsimons JF*, et al.* An integrated silicon photonic chip platform for continuous-variable quantum key distribution. *Nat Photonics* 2019, **13**(12)**:** 839-842.

46. Hickstein DD, Carlson DR, Mundoor H, Khurgin JB, Srinivasan K, Westly D*, et al.* Self-organized nonlinear gratings for ultrafast nanophotonics. *Nat Photonics* 2019, **13**(7)**:** 494-499.

47. Tran RJ, Sly KL, Conboy JC. Applications of Surface Second Harmonic Generation in Biological Sensing. *Annual Review of Analytical Chemistry* 2017, **10**(1)**:** 387-414.

48. Miller DAB. Are optical transistors the logical next step? *Nat Photonics* 2010, **4**(1)**:** 3-5.

49. Gallo K, Assanto G. All-optical diode based on second-harmonic generation in an asymmetric waveguide. *JOSA B* 1999, **16**(2)**:** 267-269.

50. Fejer MM, Magel GA, Jundt DH, Byer RL. Quasi-phase-matched second harmonic generation: tuning and tolerances. *IEEE J Quantum Electron* 1992, **28**(11)**:** 2631-2654.

Methods

Crystal growth. $NbOI_2$ single crystals were grown by chemical vapor transport. $NbOI_2$ crystals were synthesized from high-purity Nb (film), iodine (crystals) and Nb_2O_5 (powder) that were mixed to form a stoichiometric ratio Nb:O:I = 1:1:2 and sealed in the evacuated (10^{-5} mbar) quartz ampule. Sealed ampules were placed in the horizontal dual-zone furnace and brought to 600°C with the rate of 1 °C/min. The ampules were held at 600 °C for 5 days, then slowly cooled for 10 days with the slightly different rates at the hot (1.2 °C/hour) and cold (1.5 °C/hour) zones. This small temperature gradient ensured the growth of cm-size high-quality crystals near the cold end of the ampule. After the slow-cooling process, the furnace was turned off allowing the ampules to cool down naturally. Crystals were extracted from the opened ampules under inert conditions of an N_2-filled glove box and then stored for future use.

X-ray crystallographic analysis. The single crystal X-ray diffraction (SC-XRD) data were collected at room (T = 298 K) and low (T = 100 K) temperatures on a Bruker D8 Venture SC-XRD system equipped with Mo Kα radiation (λ = 0.71073 Å), KAPPA four-circle goniometer, PHOTON 100 detector (CMOS APS) and Oxford Cryostream. Data collection, integration and scaling were carried out using the Bruker APEX3 software package.[51] The frames were integrated with the Bruker SAINT software package using a narrow-frame algorithm. Data were corrected for absorption effects using the Multi-Scan method (SADABS). The structures were solved and refined using the Bruker SHELXTL Software Package, using the space group C 1 2 1, with Z = 4 for the formula unit, I_2NbO.[52] The final anisotropic full-matrix least-squares refinement was carried out on weighted F^2 values. Relevant crystal, collection and refinement data for the crystal structures of $NbOI_2$ at 298K and 100K are summarized in Supplementary Table S1. The crystallographic axes of the $NbOI_2$ crystals were identified from the SC-XRD analysis.

ARPES measurement. High-resolution ARPES measurement was performed in an ultrahigh-vacuum system under a pressure lower than 8×10^{-10} mbar. The ARPES chamber is equipped with a differentially-pumped UVS300 helium discharge lamp (SPECS GmbH) as the light source, which provides monochromatized photon energies of 21.2 eV (He-I) and 40.8 eV (He-II) through a toroidal mirror monochromator (SPECS GmbH). Here, we have used He-I as the ARPES source. The temperature of the $NbOI_2$ bulk sample was kept at 77 K during the measurement.

Spectroscopic ellipsometry. The anisotropic in-plane complex refractive indices of $NbOI_2$ were characterized through Mueller matrix spectroscopic ellipsometry (MMSE) measurements. MMSE spectra within the spectral range 6.2–0.65 eV (200–1900 nm) in steps of 20 meV were acquired using a commercial rotating analyzer instrument with a compensator (VASE, J.A. Woollam Co.). The samples were mounted on a precision rotation stage (RS40, Newport) to perform azimuth-dependent measurements, and the in-plane rotation angle ϕ was varied from 0^o to 360^o. At each in-plane orientation, data were taken at three angles of incidence a (50^o, 60^o, 70^o). Such an angle-resolved measurement scheme is necessary for accessing the entire Mueller matrix and characterizing optically anisotropic samples[53-57].

Thin sample preparation. For linear absorption and SHG characterizations, the bulk $NbOI_2$ crystals were mechanically exfoliated onto clean quartz substrates using the Scotch tape method. Atomic force microscopy (AFM) was used to measure the thickness of the exfoliated flakes. To avoid any photo-oxidation effects during the SHG measurements, the flakes were covered with a thin layer of hexagonal boron nitride (*h*-BN, <10 nm) *via* the poly (dimethyl siloxane) (PDMS) stamp-transfer method. For the field-dependent SHG measurements, $NbOI_2$ devices were prepared by transferring thin $NbOI_2$ flakes onto laterally interdigitated electrodes (IDE) *via* PDMS stamping. The IDE electrodes (Pt (70 nm)/Ti (30 nm)) were patterned on SiO_2/Si wafers (SiO_2 = 300 nm) using electron beam lithography, electron beam evaporation, and lift-off process. A transfer station with an optical microscope and a rotating stage was used to transfer the $NbOI_2$ flakes in such a way that the device's lateral electrical field is aligned with the in-plane polar axis of the transferred flakes.

Optical, electrical, and optoelectronic characterizations. The micro-absorption measurement was performed by placing the $NbOI_2$ sample between aligned microscope objectives (50X Mitutoyo, apochromat, infinity corrected), for light focusing and collection. Pulsed laser (Coherent Libra) with a fundamental wavelength of 800 nm, pulse width of ~ 50 fs, and repetition rate of 1 kHz, was focused on a sapphire crystal to generate a broadband white light. The light was passed through a 750 nm short-pass filter to eliminate the residual from the fundamental, before collimation using a parabolic mirror. The light was then sent to the objective and focused into ~ 2 μm spot for the absorption measurement. The absorption spectra were obtained by comparing the transmitted light spectra between the samples and a blank

(quartz). The spectral detection was done using a monochromator (Princeton Instrument) and a photomultiplier tube setup. For the SHG measurements, a femtosecond pulsed Yb:KGW PHAROS laser system pumping of a collinear optical parametric amplifier ORPHEUS with a LYRA wavelength extension (Light Conversion Ltd, pulse duration of 180 fs, repetition rate of 200 kHz, tunable output of 210 nm – 2200 nm) was used. The excitation beam was focused onto the sample with a 100× (NA = 0.9) air objective from Nikon (~ 1 μm^2 spot size). The spectral range of the excitation beam was tuned from 700 to 1500 nm in steps of 50 nm. The nonlinear (NL) emission was collected in a back-scattering configuration *via* the same objective, and detected with an avalanche photodiode (MPD PDM Series by PicoQuant) for imaging, or by a spectrograph (PI Acton SP2300 by Princeton Instruments) for spectral measurements. The sample was fixed to an XYZ piezo-scanner stage (Nano-Drive, Mad City Labs) to perform the sample scanning. The excitation and detection polarizations were controlled with half- or quarter-wave plates, in combination with linear polarizers. The power of the collected SHG emission was measured with a calibrated silicon photodetector (Newport), while the excitation power was characterized with a germanium photodetector (Thorlabs). A continuous-flow optical microscopy cryostat was used for the low-temperature measurements. For the electric-field switchable SHG measurements, the SHG signal was recorded while the drain−source bias (supplied by Keithley Model 6430 Sub-Femtoamp Remote SourceMeter) was swept forward and backward. The polarization−electric field ($P - E$) curve was recorded using a ferroelectric tester (Precision Multiferroic II, Radiant Technologies).

Computational methods. The ab initio density functional theory (DFT) calculations are performed using QuantumESPRESSO[58, 59] working with Perdew, Becke and Ernzerhof (PBE) optimized norm-conserving Vanderbilt pseudopotentials[60, 61]. The full relaxations of the $NbOI_2$ atomic structures are performed with Semiempirical Grimme's D3 correction[62] using the conjugate gradient scheme until the maximum residual force smaller than 1×10^{-7} a.u. and the maximum energy difference between consecutive iterations is smaller than 1×10^{-9} Ry. A kinetic energy cut-off of 80 Ry for the pseudopotential and a Monkhorst-pack k-point mesh[63] of 12×6×1 is used. A vacuum height of 12Å is added to prevent interactions between the periodic images. The GW calculation is performed with BerkeleyGW[35, 64, 65] on top of Quantum ESPRESSO with slab coulomb truncation[66], Hybertsen-Louie generalized plasmon pole model[35] and a dielectric matrix cut-off of 10 Ry. The nonuniform neck subsampling (NNS) is used to sample the reciprocal space in GW[67]. The GW quasiparticle energies are calculated

with 1536 bands, using a 12×6×1 q-mesh with another 10 q-points in the Voronoi cell around q = 0, forming an effective uniform grid of more than 120×60×1.

Data availability

The data supporting the findings of this study are available within the Article and its Supplementary Information or from the corresponding authors upon reasonable request. The X-ray crystallographic coordinates for structures reported in this study have been deposited at the Cambridge Crystallographic Data Centre (CCDC), under deposition numbers 2169918-2169919. These data can be obtained free of charge from The Cambridge Crystallographic Data Centre via www.ccdc.cam.ac.uk/data_request/cif.

References

51. Bruker Nano I. Bruker APEX3. 2019.

52. Sheldrick GM. SHELXT–Integrated space-group and crystal-structure determination. *Acta Crystallographica Section A: Foundations and Advances* 2015, **71**(1)**:** 3-8.

53. Schubert M. *Infrared ellipsometry on semiconductor layer structures: phonons, plasmons, and polaritons*, vol. 209. Springer Science & Business Media, 2004.

54. Losurdo M, Hingerl K. *Ellipsometry at the Nanoscale*. Springer, 2013.

55. Schmidt D, Booso B, Hofmann T, Schubert E, Sarangan A, Schubert M. Monoclinic optical constants, birefringence, and dichroism of slanted titanium nanocolumns determined by generalized ellipsometry. *Applied Physics Letters* 2009, **94**(1)**:** 011914.

56. Schmidt D, Booso B, Hofmann T, Schubert E, Sarangan A, Schubert M. Generalized ellipsometry for monoclinic absorbing materials: determination of optical constants of Cr columnar thin films. *Optics Letters* 2009, **34**(7)**:** 992-994.

57. Schubert M. Polarization-dependent optical parameters of arbitrarily anisotropic homogeneous layered systems. *Phys Rev B* 1996, **53**(8)**:** 4265-4274.

58. Giannozzi P, Baroni S, Bonini N, Calandra M, Car R, Cavazzoni C*, et al.* QUANTUM ESPRESSO: a modular and open-source software project for quantum simulations of materials. *Journal of Physics: Condensed Matter* 2009, **21**(39)**:** 395502.

59. Giannozzi P, Andreussi O, Brumme T, Bunau O, Buongiorno Nardelli M, Calandra M*, et al.* Advanced capabilities for materials modelling with Quantum ESPRESSO. *Journal of Physics: Condensed Matter* 2017, **29**(46)**:** 465901.

60. Hamann DR. Optimized norm-conserving Vanderbilt pseudopotentials. *Physical Review B* 2013, **88**(8)**:** 085117.

61. Perdew JP, Burke K, Ernzerhof M. Generalized Gradient Approximation Made Simple. *Physical Review Letters* 1996, **77**(18)**:** 3865-3868.

62. Grimme S. Semiempirical GGA-type density functional constructed with a long-range dispersion correction. *Journal of Computational Chemistry* 2006, **27**(15)**:** 1787-1799.

63. Monkhorst HJ, Pack JD. Special points for Brillouin-zone integrations. *Physical Review B* 1976, **13**(12)**:** 5188-5192.

64. Rohlfing M, Louie SG. Electron-hole excitations and optical spectra from first principles. *Physical Review B* 2000, **62**(8)**:** 4927-4944.

65. Deslippe J, Samsonidze G, Strubbe DA, Jain M, Cohen ML, Louie SG. BerkeleyGW: A massively parallel computer package for the calculation of the quasiparticle and optical properties of materials and nanostructures. *Computer Physics Communications* 2012, **183**(6)**:** 1269-1289.

66. Ismail-Beigi S. Truncation of periodic image interactions for confined systems. *Physical Review B* 2006, **73**(23)**:** 233103.

67. da Jornada FH, Qiu DY, Louie SG. Nonuniform sampling schemes of the Brillouin zone for many-electron perturbation-theory calculations in reduced dimensionality. *Physical Review B* 2017, **95**(3)**:** 035109.